FACTA UNIVERSITATIS
Series: **Mechanical Engineering**
https://doi.org/10.22190/FUME230405019A

Original scientific paper

EFFECT OF ISOTHERMAL AND ISOCHRONAL AGING ON THE MICROSTRUCTURE AND PRECIPITATE EVOLUTION IN BETA-QUENCHED N36 ZIRCONIUM ALLOY

Ali W. Aldeen[1,2], Dina Y. Mahdi[2], Chen Zhongwei[1], Imad A. Disher[3], Barhm Mohamad[4]

[1]State Key Laboratory of Solidification Processing, Northwestern Polytechnical University, Shaanxi, China
[2]Department of Materials Engineering, College of Engineering, University of Kufa, Najaf, Iraq
[3]Department of Ceramics and Building Materials, College of Materials Engineering, University of Babylon, Babil, Iraq
[4]Department of Petroleum Technology, Koya Technical Institute, Erbil Polytechnic University, Erbil, Iraq

Abstract. *In this study, the effect of isothermal and isochronal aging is reported to investigate the precipitate evolution and recrystallization of N36 zirconium alloy after β-quenching. Two groups of samples were cut from the as-received sheet of N36 zirconium alloy and subjected to solution treatment and subsequent aging at 580, 640, and 700 °C for 40 and 600 min, respectively. Optical microscopy (OM), scanning electron microscopy (SEM), transmission electron microscopy (TEM), energy dispersive spectroscopy (EDS), and electron backscattering diffraction (EBSD) were utilized to characterize the microstructure and second-phase particle (SPPs) evolution. Results show that the implemented quenching after solution treatment produces fine interlaced α-plates structure conserved inside prior β grain boundaries with 12 variant directions that follow Burger misorientation characteristics. After aging for a short time, initial α-plates conserve their shape and become softer, and SPPs spread along their boundaries. Recrystallizations are finished for specimens aged at a higher temperature or for a longer time. The recrystallized structure exhibits non-uniform grains and a random SPPs distribution. Despite the differences in morphology, some recrystallization grains retain the orientation feature from the initial α-plates. Hardness declines as temperature and time rise, and no hardness peak is seen. Roughness and wettability rise with increasing ageing temperatures.*

Key words*: N36 zirconium alloy, Aging, Second phase particles, Recrystallization*

Received: April 05, 2023 / Accepted June 24, 2023
Corresponding author: Zhongwei Chen
State Key Laboratory of Solidification Processing, Northwestern Polytechnical University, Xi'an, 710072, Shaanxi, China
E-mail: chzw@nwpu.edu.cn

1. INTRODUCTION

The corrosion resistance and mechanical properties of zirconium alloys depend on the features of their microstructure, which include those of the parent phase as well as those of the second phase particles. The presence of the second phase particles may not only promote the nucleation of recrystallized grains during the annealing process but also hinder the migration of grain boundaries during recrystallization and grain growth. Therefore, it is of great scientific and engineering significance to study second phase precipitation behavior along with the development of the microstructure of zirconium alloys [1, 2].

It is well known that the chemical composition plays a vital role in the development of the microstructure of an alloy and determines its response to heat treatment during manufacturing processes. The optimal compositions for novel zirconium alloys have thus been the subject of numerous research efforts [1–5]. At present, in the process of deepening burnup and prolonging the refueling cycle life, a large number of Nb-containing alloys are used as fuel element cladding. Among these new alloys, N36 was independently developed in China from the Zr-Sn and Zr-Nb series.

To obtain a zirconium alloy with specific properties and performance that meet the requirements of cladding applications, a detailed study of the microstructure is indispensable. Many efforts have been made in the past few years to study the microstructure of SPPs; these include the phase identification of SPPs in pre-deformed and annealed alloys [6–8], the chemical composition, and the crystal determination of SPPs [9-12]. Studies have also looked at how microstructure evolution alters mechanical properties [13-16]. However, studying the effect of SPPs distribution on the recrystallization process during the heat treatment is still under consideration due to the lack of research coverage on this topic.

The production process of N36 alloy sheet is passed through: ingot β-phase quenching, α-phase hot rolling, several intermediate annealing's, 30%-50% cold working after each annealing is finished, and final annealing to proceeds recrystallization [17]. Heating into the β phase and then cooling rapidly to room temperature makes the microstructure of zirconium alloy very complex, and it is expected that the martensitic structure will be formed during very rapid cooling. The matrix resulted in super saturation with alloying elements [18,19]. Therefore, the processes of recrystallization and precipitation will be more complicated during the further thermal treatment that follows β-quenching. Chai et al. [20] studied the effect of aging temperatures in the range 600-700°C in different periods of time on Zr-0.85Sn-0.4Nb-0.4Fe-0.1Cr-0.05Cu alloy. They found a linear distribution of SPPs on the boundary of α-plates after a short time and low temperature of aging, while as temperature or time increases, heterogeneity of both recrystallization and the random distribution of SPPs occurs. On the other hand, Gopalan et al. [21] performed positron annihilation measurements to study the aging response of β-quenched Zircaloy-2. By detecting positron lifetime and the S-parameter, they have tried to correlate those defect-sensitive signals to various microstructural features. Jayakumar et al. [22] used 2-100 MHz ultrasonic attenuation and velocity measurements to test the hard intermetallic in β-quenched Zr-2 during aging. Velocity measurements were found to be more dependable and repeatable for characterizing Zircaloy-2 microstructure than attenuation measurements.

In the current study, the effect of aging following β-quenching on the recrystallization and precipitation behavior of N36 alloy with Nb as the dominant element was mainly

investigated. This is of crucial importance in order to understand the relationship between the microstructure and the aging heat treatment, provide practical guidance for the evolution of SPPs distribution, and find the relation between grain orientation prior to and following recrystallization, the mechanism through which precipitation and recrystallization are interacted, and their effect on hardness, roughness, and wettability.

2. EXPERIMENTAL METHOD

Fully recrystallized sheet material of N36 zirconium alloy provided by the China Nuclear Power Institute with a chemical composition of Zr-0.85Sn-1Nb-0.3Fe-0.1O (wt.%) is used in current work. The original sheet was cut into a group of samples measuring 10 mmx6 mmx1 mm. In order to prevent oxidation during heating, the samples were sealed in a vacuum glass tube with $4.7x10^{-3}$ Pa. Firstly, all samples were subjected to β solution treatment at 1050°C for a holding time of 35 min; after that, the samples were quenched in cold water immediately after crushing the vacuum tube and denoted as WQ. Then, the samples were aged at 580, 640, and 700°C for 40 min and 600 min, respectively. The samples with a 40 min holding time are denoted as 580A, 640A, and 700A, while the samples with a 600 min holding time are denoted as 580B, 640B, and 700B, as shown in Fig. 1.

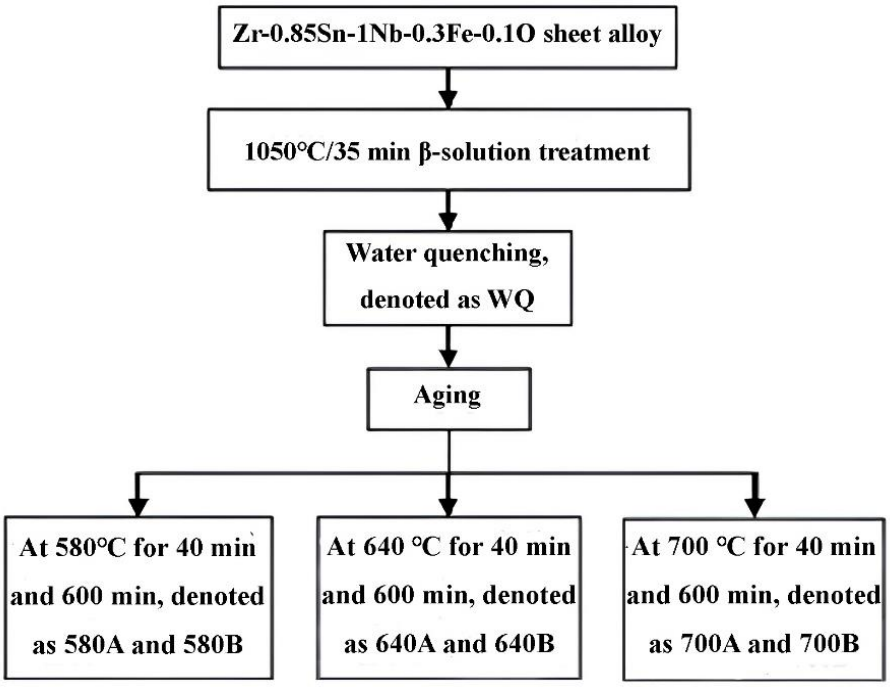

Fig. 1 Schematic representation of heat treatment

The microstructures of the samples in both groups were characterized using an optical microscope (OM) and the SEM secondary electron (SE) image. For OM and SEM observation, the samples were gradually polished using SiC papers with a final grit number of 5000, and after that, they underwent chemical etching using a solution of H_2O, HNO_3, and HF as etching agents prepared in a ratio of 45:45:10. FEI Tecnai G2 F20 SuperTwin transmission electron microscopy with an accelerating voltage of 200 kV was used to obtain some results. An energy-dispersive X-ray spectroscopy (EDS) equipped with TEM to get the chemical identification of some particles. Conventional twin-jet polishing was used as a surface preparation technique for the TEM imaging with a mixed solution of 90% ethanol and 10% perchloric acid below -35°C. An electron backscatter diffraction (EBSD) system is also equipped with a SEM system to characterize the microstructure of some aging samples. The electrochemical polishing parameters used for EBSD sample preparation were 20 V voltages, 0.4-0.6 A current, and a polishing time of 10-40 S. In order to ensure the validity of the statistical results, at least 300 second phase particles were counted for each aged sample. A Vickers indentation machine (DHV-1000 hardness tester model) was used to measure hardness in each state. The average result of ten indentations on each surface of the sample was adopted, and the loading force of the hardness tester was 9.8 N with a loading time of 15 s. An atomic force microscope (AFM, NTEGRA from NT-MDT), an optical contact angle meter, and interfacial tension were used to evaluate surface properties.

3. Experimental Results

3.1 β-Quenched Microstructure

Figure 2a shows an optical micrograph image of N36 alloy after solution treatment and quenching in cold water. The high temperature β phase converted to a fine interlaced α-plates structure with different crystalline orientations that were surrounded by prior β-grain boundaries, indicating the growth trends of the α-plates. Such a fine plate with a thickness of about 1μm results from a high cooling rate [19]. Figure 2b represents a bright field (BF) TEM image of β-quenched sample. Three evidences can be drawn, the first of which is the absence of precipitate, which indicates the super saturation of alloying elements inside the matrix; the second is the irregularity of the grain boundaries; and lastly, the presence of large dislocations, which indicates that the energy is high, which will encourage the precipitate to nucleate and grains to recrystallize to reach the state of stability during further thermal processes. Figure 2c is an inverse pole figure (IPF) EBSD image showing the crystallographic orientation of the α-plates inside a large β-grain boundary, with each color indicating that α-plates have different orientations. Combined with Figure 2a, it can be found that α-plates clusters in the same direction have the same color and, therefore, the same crystallographic orientations. Using the misorientation angle distribution MAD in Fig. 2d, it can be obtained that a large number of α-plates are gathered around 60°, and at the same time, there is a relatively small amount aggregated around 10° and 90°. The existence of such a special distribution is due to Burger's relation, where a single β grain can give 12 α variants directions [23].

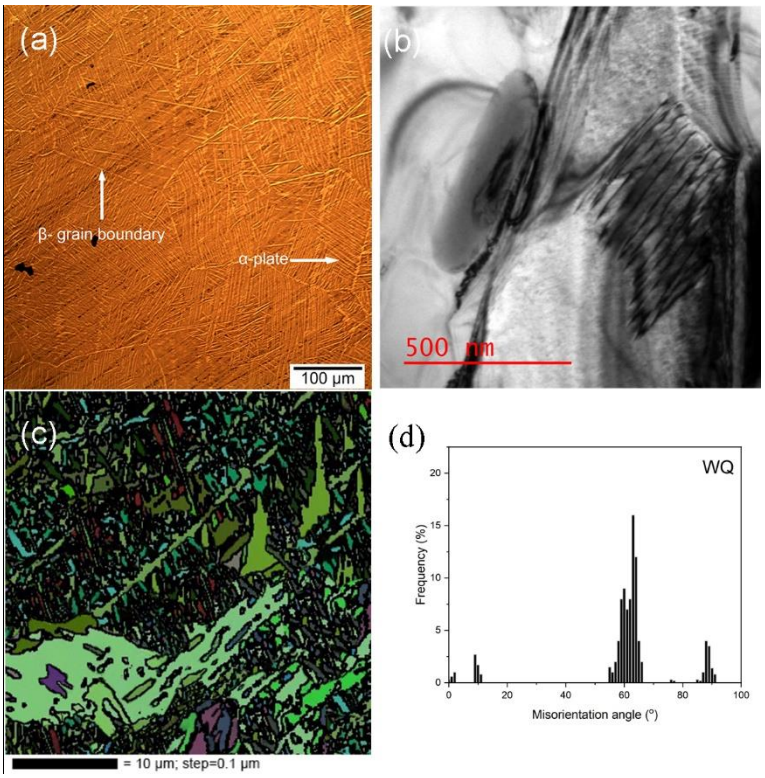

Fig. 2 β-quenching microstructure: (a) optical micrograph (b) BF-TEM image (c) EBSD-IPF Image (d) MAD histogram

3.2 Recrystallization and SPPs evolution during aging

Figure 3 shows a group of images for samples aged at 580-700°C after β-quenching. According to samples aged for a short time (group A), it seems that the time is very short to induce the recrystallization process even at high temperatures of 700°C, and the α-plates structure kept well. As time prolongs in group B, a change in the microstructure becomes apparent compared with the initial β-quenching state. Some ancient interlaced α-plates still kept in the 580B sample beside the new recrystallization microstructure, while samples 640B and 700B showed an almost striking change of structure towards recrystallization.

Figures 4a and 4b represent BF-TEM images of 640A and 640B aged samples, respectively. Fig. 4a shows that the α-plates structure is still conserved with regular plate boundaries compared with that in β-quenching, see Fig. 2b, with less dislocation area, which indicates that with a short aging time, α-plates are oriented towards dynamic recovery. Also, there is some small precipitate scattered along the plate's boundaries, which proves that aging has indeed exerted a significant influence on the β-quenching microstructure. On the other hand, in Fig. 4b striking changes in morphologies occur compared with the β-quenching microstructure. In this figure, the interlaced α-plate is totally replaced by an irregular grain shape with SPPs distributed randomly both inter- and intra-granularly. Another phenomenon that should be noticed is that the precipitate on the

grain boundaries is larger than that inside the grains, following the Ostwald ripening mechanism [19]. A high magnification BF-image in Fig. 4c (integrated with Fig. 4b) confirmed a hexagonal closed-packed structure with ellipsoidal morphology of SPP as the almost nature of the precipitate.

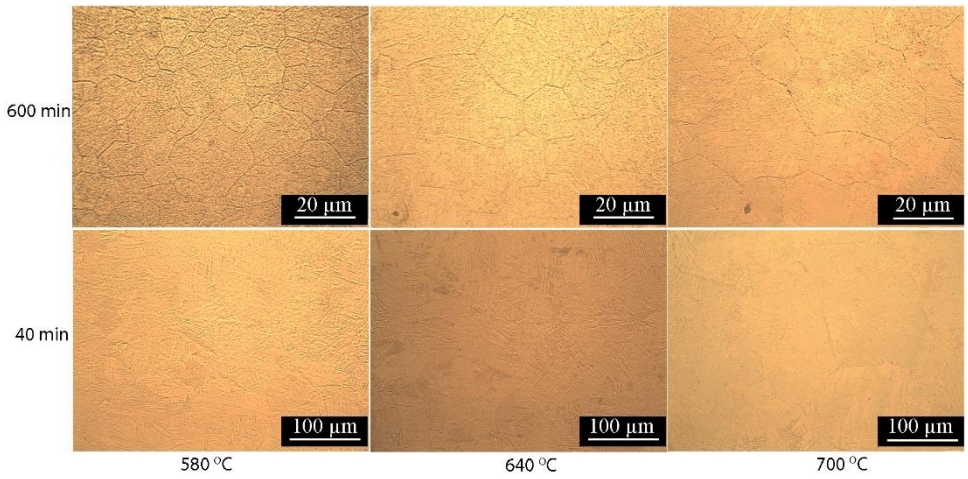

Fig. 3 Optical micrograph of microstructure development for samples aged at different times and temperatures

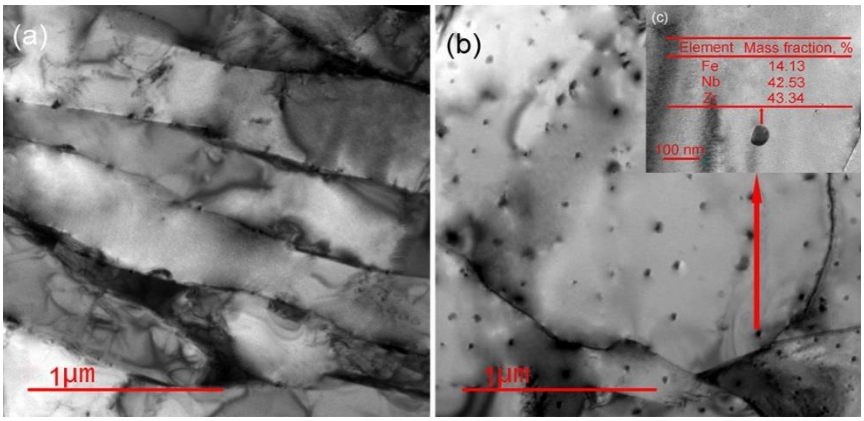

Fig. 4 BF-TEM comparison images of microstructure for (a) 640A sample (b) 640B sample (c) SPP chemical identification

The SPPs distribution results are shown in Fig. 5. For samples aged in group A, SPPs are distributed linearly, noting that, as the temperature increases, the particle size increases a little, as does the transverse distance between lines. For group B, SPPs are distributed randomly, and as the temperature increases, the particles size apparently increases. The general shape of the SPPs is semi-spherical in the early stages of precipitation, indicating the formation of GP zones, i.e, the precipitates are fully coherent with the parent phase. As

the temperature or time increases, their shape becomes polyhedral, indicating the loss of coherency with the parent phase [24], and tends to coarsen, as shown in the histogram of Fig. 6.

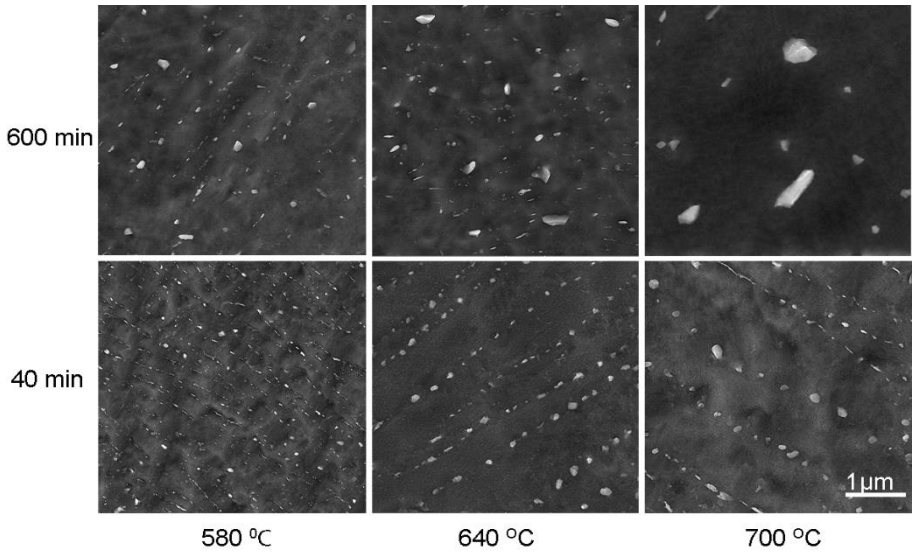

Fig. 5 SPPs morphology and distribution after aging of samples A and B

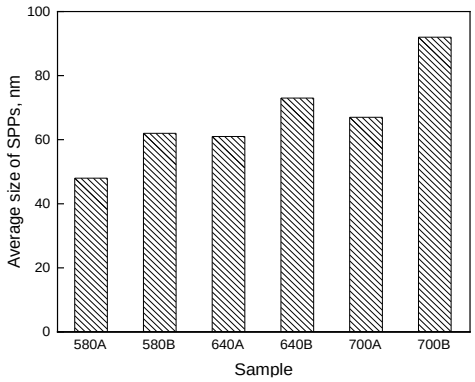

Fig. 6 Average size of SPPs in different aging samples

Fig. 7a represents the IPF-EBSD image and the related misorientation information shown in Fig. 7b after aging sample 580B. According to the result of the microstructure, two regions can be observed separately: still conserved -plates obtained by β-quenching that need more driving force to overcome the high stress in those regions, and recrystallized structure in some grains inside huge prior β-grain boundaries. The misorientation angle in Fig. 7b is almost identical to the features of misorientation distribution inherited from β-quenching, where the misorientation information is distributed in the same way as on parent plates. Finally, some small grains recrystallized inside massively recrystallized grains.

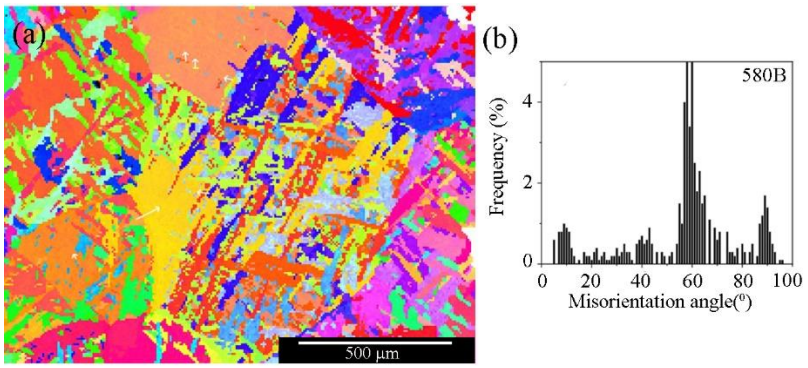

Fig. 7 IPF-EBSD image of (a) 580B aged sample (b) corresponding MAD

Fig. 8 shows the IPF-EBSD and misorientation distribution histogram after aging sample 640B. From the figure, one can see that striking changes in morphologies occur compared with the β-quenching microstructure. All β-quenching microstructures totally disappear and are replaced by recrystallization characteristics as clearly visible, where the small recrystallized grains are almost sited near the β-boundary while the large grains grow inside it. Another phenomenon one should notice is that the recrystallized grains are inhibited from penetrating the β-grain boundary. One can conclude from Figs. 7(a) and 8(a) that, as the aging temperature increases, the driving force continues to grow protrusion small grain boundaries and convert them to small recrystallized grains while the previous recrystallized grains continue in their growth. Also, the size of the recrystallized grains well reflected the effects of precipitates on their size. In addition, despite the stark change in morphologies, the MAD data from EBSD shows that the recrystallized structure still carries over some characteristics from the β-quenching structure, as illustrated in Fig. 8(b). However, it appears that the maximum density has been significantly reduced as a result of the spread of other misorientations following recrystallization.

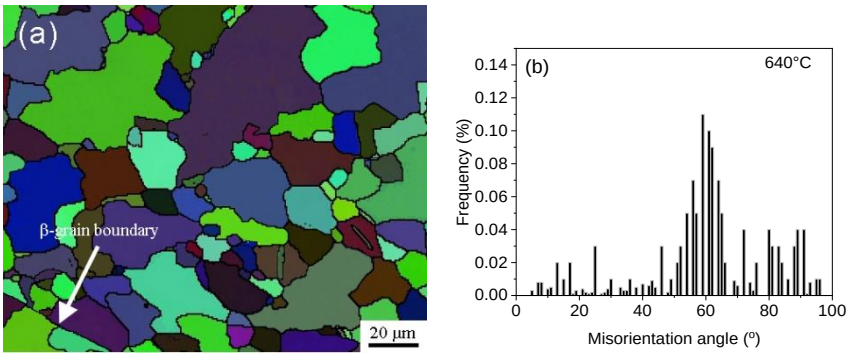

Fig. 8 640B aging sample (a) IPF-EBSD image (b) MAD histogram

3.3 Micro-hardness, AFM and wettability testing

To better reveal the effect of microstructure and precipitate evolution on surface characterizations of N36 zirconium alloy during the aging process, Vickers micro-hardness, AFM, and wettability tests were performed.

The degree of specimen hardness can serve as a reflection of the simultaneous processes of precipitation and recrystallization during ageing. The results of average Vickers micro-hardness are shown in Fig. 9 for both β-quenching and aged samples. It can be seen that the hardness graph lines show a decrease in values from β-quenching to increasing time at any fixed aging temperature. Even at low temperatures, there is no hardness peak. Therefore, the hardness values decrease as the recrystallization proceeds in the samples. Note that sample 700B shows some inconsistency in its value despite the progress of its recrystallization process. Another incidence that should be noted is that the hardness values of group A samples decreased even though they conserved the plate structure at a lower aging time compared to the hardness of β-quenching sample.

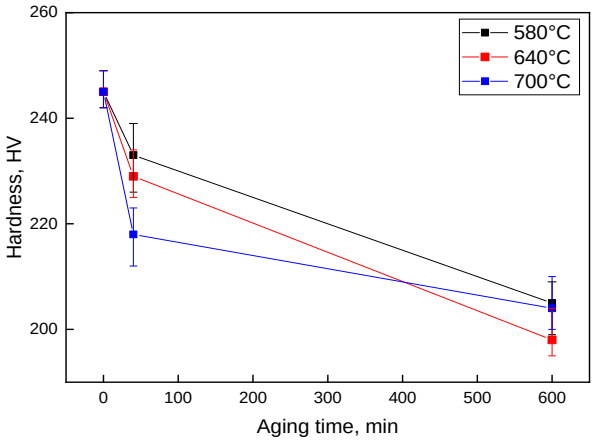

Fig. 9 Vickers micro-hardness results of β-quenching and aging samples

Due to the AFM's ability to detect height variations on the sample in the range of nanometers, this method is excellent for showing the impact of SPPs changes in surface topography. Fig. 10 shows 2D and 3D AFM results of surface characterization in the 10x10 μm^2 scan area of β-quenching and 580B and 700B aging samples after polishing, cleaning, and drying the surface to reduce the influence of surface defects during the heating and quenching processes. The β-quenching surface is essentially featureless, though some mounts or pits with an average roughness (Ra) below 2 nm are still present, as shown in Fig. 10 (a, b). In comparison, the Ra of aging surface samples confirms a slight increase in roughness due to the precipitation of particles during the aging process. The surface roughness increased from 2 nm in β-quenching sample to 8.7 and 13.4 nm in the 580B and 700B aging samples, as shown in Fig. 10 (c, d) and (e, f). A small protrusion, located within a black circle, could be seen on the surface of the 700B-aged sample in Fig. 10 (e, f).

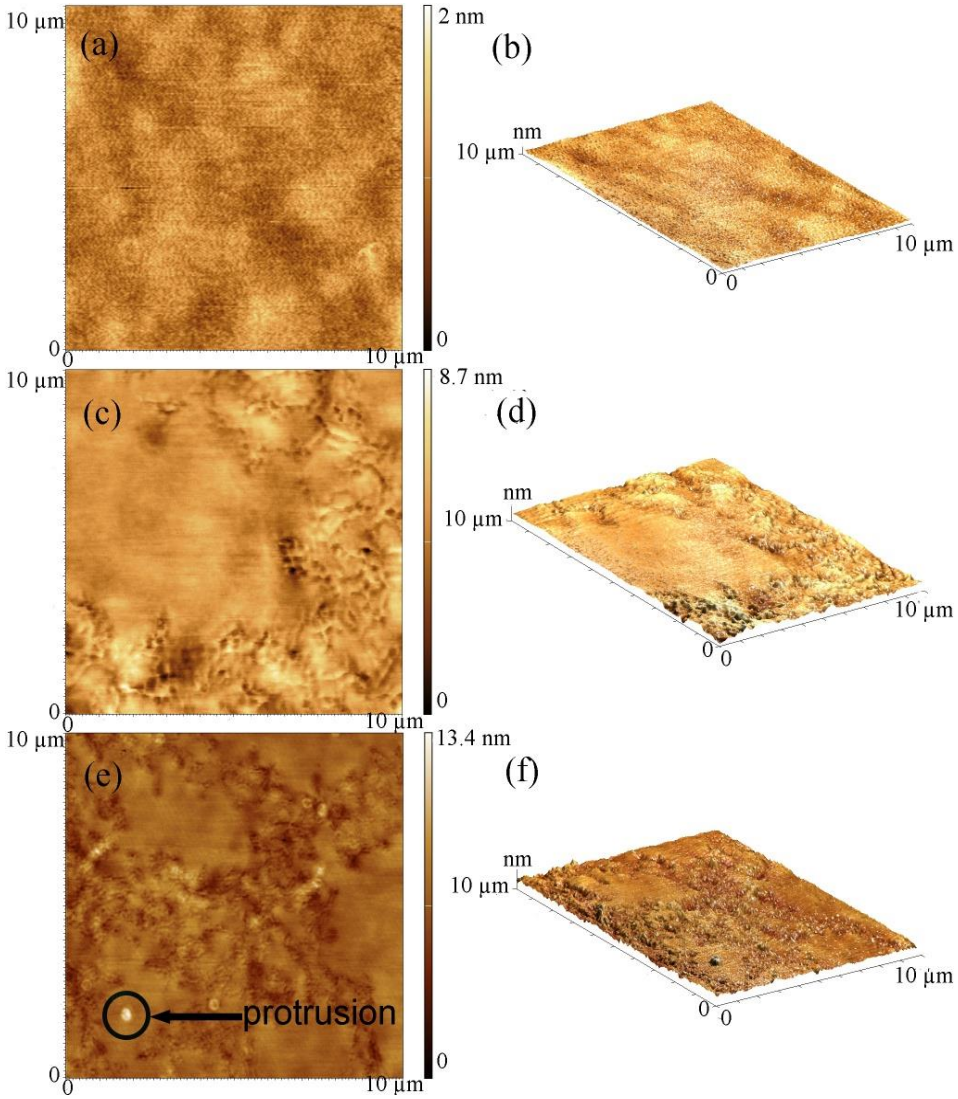

Fig. 10 2D and 3D AFM micrograph images: (a-b) β -quenching sample; (c-d) 580B; (e-f) 700B

Figure 11 shows the contact angle results of a microliter droplet on the β-quenching, 580B, and 700B surfaces. It can be seen clearly that the shape of ultrapure water droplets on all surfaces did not change much after aging compared with that of β-quenching, all droplets show a hydrophilic property; and the contact angle decreased from 70.26° in β-quenching substrate to 63.25° in 580B substrate and 57.16° in 700B substrate. Therefore, the surface's wettability increased after aging.

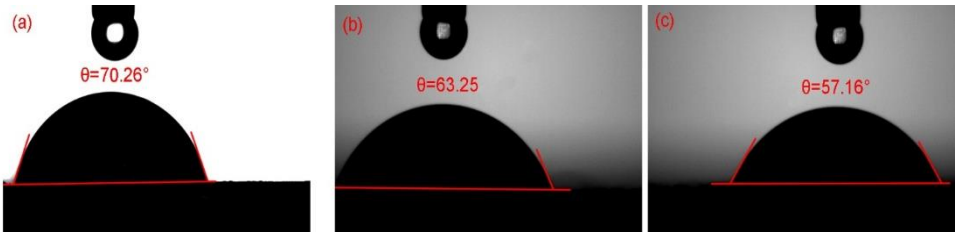

Fig. 11 Contact angle test of three surface: (a) β-quenching substrate; (b) 580B substrate; (c) 700B substrate

4. DISCUSSION

4.1 β-quenching microstructure

The appearance of such a fine interlaced α-plates structure in Figs. 2a and 2c is essentially due to rapid quenching immediately after solution treatment. Previous studies [23] confirmed that the rapid cooling from the β-solution treatment region for zirconium alloys containing β-stabilizer elements larger than α-stabilizer could induce such a fine martensitic structure. In addition to the large number of defects that are introduced during the rapid cooling process, including vacancies, dislocations, and interfaces, the alloying elements are also saturated in matrix. The misorientation distribution of the interlaced α-plates obeys strictly burger relationship shear transformation during transformation from β to α. Burger suggested that 12 α variants could arise from prior β parent grain based on the symmetry of both phases. All burger distributions appeared during the results; these values precisely take place only at 10°, 59°-64°, and 90° [23]. The weaker frequency distribution of α-plate at 10° and 90° could be attributed to difficult coverage over a large area by the EBSD test, specifically with a complex α-plate structure. Some small grains deviate from the burger distribution values. This could be due to an error during testing.

4.2 Precipitate and grain growth relationship during aging

The rapid cooling rate produces a high driving force stored inside the β-quenching structure. This driving force will release and have the priority of contributing to the recrystallization of the alloy matrix during the subsequent aging to reduce the surface energy. During aging, the alloying elements in their supersaturated state in the matrix will also be polarized and eventually precipitate as second-phase particles to reduce the energy of the system. Couet et al. [25] studied the transformation kinetics of ZR-4 alloy during aging after water quenching by TEP. The results showed that the full precipitation of the second phase always occurs earlier than the recrystallization in the single α-phase region. Additionally, a study by Garner et al. [26] showed that the second phase of the ZR-4 alloy was fully separated after aging at 610°C for only 1 min. When the aging temperature of 580°C was used, the precipitation of the second phase particles also preceded the recrystallization process. In our previous study [19], the growth kinetics of SPPs calculated after aging of the current alloy, and the results show agreement with the fact that the precipitation of the second phase particles preceded the recrystallization process during aging. All previous studies give a good explanation of why SPPs are distributed linearly at

α-plate grain boundary during aging for a short time. Therefore, after β-quenching a large amount of α-plates boundaries is produced, and the prior β-grain boundaries are still kept well. The second phase will have priority for nucleation at such sites due to the smoothing of the nucleation path. So, the linear distribution of SPPs on α-plat boundaries begins to be more apparent for short-period aging. After prolonged aging time, the recrystallization will proceed and make the SPPs distributed inter- and intragranularly. However, big particles will coarsen at the grain boundary under the conditions of the Ostwald repining mechanism [19].

With extended aging time, the recrystallization process will expand into nearby regions with larger dislocation densities after they have formed. After aging the 580B sample, two sites were observed to be well divided into those that still conserved the initial α-plates and the preferred recrystallization zone starting from the prior β-grain boundary. While, regarding the 640B and 700B samples, α-plate structure disappeared and changed to fully recrystallized grains. Luan et al. [18] found that 2 and 4 hours are not enough to induce a fully recrystallized state during the aging of zr-4 alloy at 650 °C; instead, it takes about 72 hours to obtain a fully recrystallized state. In the current investigation, 10 h is enough time to induce a fully recrystallized structure at 640°C, or it may be less. Chai et al. [20] found 90 min to be enough time to complete recrystallization at 650°C in Zr–0.85Sn–0.4Nb–0.4Fe–0.1Cr–0.05Cu alloy and gave a good explanation. Although water quenching is still a common factor in the starting state, the variation in cooling rate may still exist due to the difference in sample size in the working condition.

According to the irregular shape of recrystallized grains, it is known that the high cooling rates induce the formation of dense dislocation, as seen in Fig. 2b, which will assist α-plates boundaries in migration during the recrystallization process. Strain-induced boundary migration (SIBM) with dislocation density is suggested as a responsible mechanism for inducing the recrystallization process and the production of massive grains by Rumball and Coleman. [9]. During recrystallization, the early precipitated particles have a big effect on the recrystallization process [27]. When the α-plates boundary moves to recrystallize, it meets the precipitated particles and is affected by Zener pinning resistance (Pz) [28]. If the driving force of recrystallization is greater than Pz, the grain boundary can continue to advance around the second phase particles. If at a particular location the driving force is less than Pz, the grain boundary will be pinned in its original direction and continue to grow in the direction of smaller resistance. Therefore, movement of recrystallized grain boundaries in association with many defect dispersions in the matrix towards the distribution of second phase particles leads to interaction, eventually forming a highly irregular shape of the grain.

On the other hand, when the boundary of α-plates moves towards the prior β-Zr grain boundary during recrystallization, it collides with a large number of SPPs stationed there, since these places are the preferred sites for the growth of such particles due to the smooth route of nucleation. So Pz was much larger than the recrystallization driving force, and eventually the recrystallized grains still took the original β-Zr grain boundary as part of the grain boundary. Thus, these particles will be responsible for obstructing the boundary of α-plates and preventing them from penetrating the prior β grain boundary during recrystallization [29, 30].

Regarding the relatively good agreement between the inherited misorientation angle distribution after recrystallization and that in β-quenching state according to the concept of burger [23], Chai et al. [20] found that the misorientation distribution inherited from the

two states of β-quenching and recrystallization is also almost the same in both, with a relatively weak frequency in the recrystallization state. Therefore, the growth of the plate structure during recrystallization is almost in the same preferred direction.

4.3 Effect of solution treatment and aging on hardness, roughness and wettability

In agreement with previous studies [20, 31], the hardness values decreased during the aging process compared with those in the β-quenching state, which has a maximum value of 245 HV. When samples are aged for a short time, the hardness values decrease, although the samples still conserve the α-plate structure and induce SPPs nucleation. The decrease in hardness caused by the recovery process and changes in texture. During extended aging periods, the decrease in hardness becomes more pronounced. A slight increase in the hardness value of the 700B sample could be due to the coarsening of SPPs at this stage. Generally, the main purpose of the alloying elements in zirconium alloy is still highlighted as improving corrosion resistance rather than the mechanical properties of the alloy [10,32].

The surface topography of the β-quenching, 580B, and 700B samples confirmed the presence of a slight increase in the surface roughness despite the use of the vacuum tube glass protection during heating [33]. The difference in the surface topography is mainly related to the absence of SPPs in the β-quenching sample and their presence in the aging samples [34]. The increase in the size of the protrusions is probably due to the increase in the size of the oxidized SPPs compared to the oxidized surface due to the migration of the alloying elements to the free surface and then oxidation [35]. Hence, the increasing Ra values between 580B and 700B aged samples are attributed to the increasing size of the SPPs underneath the surface and their concentration and oxidation in a specific place.

Regarding contact angle results, the surface wettability increased with increasing aging temperature, in agreement with increasing surface roughness. Therefore, it's possible that the SPPs size contributed to the surface roughness and played the same role in increasing surface wettability, where increasing particle size leads to an increase in surface wettability. Also, it is stated that fine SPPs improve corrosion resistance compared to coarse SPPs [2, 36]. Based on what was discussed, coarsening SPPs leads to increased surface wettability.

5. CONCLUSION

Due to the significance of thermal treatment during the manufacturing process, the effect of isothermal and isochronal aging following β-quenching on the microstructure and SPPs evolution of N36 zirconium alloy is investigated. Some important conclusions are as follows:

1. After β-quenching, the results show a structure of interlaced α-plates that follows Burger orientation distribution, and the supersaturating of the alloying elements in the matrix are the main characteristics of this stage.

2. For a short aging period, α-plates structure is well conserved in all temperature ranges (580°C–700°C), and the SPPs distributed linearly in the boundary of α-plate structure. With increasing aging temperatures, the size of the particles increases.

3. For longer aging time, the 580B sample show two regions; still kept α-plate and recrystallized grains, while in 640B and 700B, α-plates disappeared and totally changed to irregular recrystallized grain. Some grains that have undergone recrystallization have

successfully inherited the misorientation distribution characteristic of α plates. In addition, the large size of SPPs sited on the prior β-grain boundary prohibited α-plate from penetrating during recrystallization.

4. The hardness values decreased from their maximum value in the β-quenching state during the aging process. A slight increase in the hardness value of the 700B sample could be due to the coarsening of the precipitate.

5. Although under a controlled atmosphere of aging, a fractional change in roughness and wettability of tested substrates occurred because of SPPs development.

Acknowledgement: *The authors gratefully acknowledge financial support from National Key R&D Program of China (NO.2018YFB1900100), and the Nuclear Power Institute of China for the N36 Zr alloy sheet. Special thanks to Mr. Erik Nilsson in his cooperation for this work.*

REFERENCES

1. Yang, S., Guo, Z., Zhao, L., Zhao, L., Guan, Q., Liu, Y., 2019, *Surface microstructures and high-temperature high-pressure corrosion behavior of N18 zirconium alloy induced by high current pulsed electron beam irradiation*, Appl. Surf. Sci., 484, pp. 453-460.
2. Liu, W., Li, Q., Zhou, B., Yan, Q., Yao, M., 2005, *Effect of heat treatment on the microstructure and corrosion resistance of a Zr–Sn–Nb–Fe–Cr alloy*, J. Nucl. Mater., 341, pp. 97-102.
3. Alat, E., Motta, A.T, Comstock, R.J., Partezana, J.M., Wolfe, D.E., 2015, *Ceramic coating for corrosion (c3) resistance of nuclear fuel cladding*, Surf. Coatings Technol., 281, pp. 133-143.
4. Dekhtyar, A.I., Bondarchuk, V.I., Karasevska, O.P., Oryshych, D.V., Savvakin, D.G., Skoryk, M.A., 2019, *Microstructure change under hot deformation in zirconium alloys synthesized by powder metallurgy*, Mater. Charact., 158, 109949.
5. Kim, J.H., Lee, M.H., Choi, B.K., Jeong, Y.H., 2007, *Effect of the hydrogen contents on the circumferential mechanical properties of zirconium alloy claddings*, J. Alloys Compd., 431, pp. 155-161.
6. Chen, L., Li, J., Zhang, Y., Lu, W., Zhang, L.C., Wang, L., Zhang, D., 2016, *Effect of low-temperature pre-deformation on precipitation behavior and microstructure of a Zr-Sn-Nb-Fe-Cu-O alloy during fabrication*, J. Nucl. Sci. Technol. 53, pp. 496-507.
7. Chai, L., Luan, B., Murty, K.L., Liu, Q., 2013, *Effect of predeformation on microstructural evolution of a Zr alloy during 550-700 °c aging after β quenching*, Acta Mater., 61, pp. 3099–3109.
8. Fan, Q., Yuan, B., Xie, M., Shi, M., Zhou, J., Yang, Z., Zhao, W., 2019, *Effects of hot rolling temperature and aging on the second phase particles of Zr-Sn-Nb-Fe zirconium alloy*, Nucl. Mater. Energy, 20, 100700.
9. Aldeen, A.W., Chen, Z., Disher, I.A., Yan, K., Zhu, Y., 2022, *Study of Initial β-Zr Formation in β-Quenched N36 Zirconium Alloy Using Dynamic and Metallographic Methods*, Crystals. 12, 1535.
10. Tao, B., Qiu, R., Zhao, Y., Liu, Y., Tan, X., Luan, B., Liu, Q., 2018, *Effects of alloying elements (Sn, Cr and Cu) on second phase particles in Zr-Sn-Nb-Fe-(Cr, Cu) alloys*, J. Alloys Compd., 748, pp. 745-757.
11. He, G., Liu, J., Li, K., Hu, J., Mir, A.H., Lozano-Perez, S., Grovenor, C., 2019, *Investigating the stability of second phase particles in Zr-Nb alloys under irradiation*, J. Nucl. Mater., 526, 151738.
12. Liu, Y., Qiu, R., Luan, B., Hao, L., Tan, X., Tao, B., Zhao, Y., Li, F., Liu, Q., 2018, *TEM study on a new Zr-(Fe, Cu) phase in furnace-cooled Zr-1.0 Sn-0.3 Nb-0.3 Fe-0.1 Cu alloy*, J. Nucl. Mater., 504, pp. 79-83.
13. Yang, H.L., Kano, S., Matsukawa, Y., Li, Y.F., Shen, J.J., Zhao, Z.S., Li, F., Satoh, Y., Abe, H., 2016, *Study on recrystallization and correlated mechanical properties in Mo-modified Zr-Nb alloys*, Mater. Sci. Eng. A., 661, pp. 9-18.
14. Lee, H., Min Kim, K., Kim, J.S., Kim, Y.S., 2020, *Effects of hydride precipitation on the mechanical property of cold worked zirconium alloys in fully recrystallized condition*, Nucl. Eng. Technol., 52, pp. 352-359.
15. Guo, W., Li, G., Yuan, F., Han, F., Zhang, Y., Ali, M., Ren, J., Yuan, G., 2021, *Texture development and mechanical behavior of Zircaloy-4 alloy plates fabricated by cold rolling and annealing*, Mater. Sci. Eng. A., 807, 140846.
16. Tewari, R., Srivastava, D., Dey, G.K., Chakravarty, J.K., Banerjee, S., 2008, *Microstructural evolution in zirconium based alloys*, J. Nucl. Mater., 383, pp. 153-171.
17. Li, Z.K., Zhou, L.A., Zhang, H.J., Wang, W.S., Jin, Z.H., 2004, *The existing form of Nb in Zr-Sn-Nb-Fe alloys and its dependence on intermediate annealing*, Rare Met. Mater. Eng., 33, pp. 1362-1364.

18. Luan, B.F., Chai, L.J., Chen, J.W., Zhang, M., Liu, Q., 2012, *Growth behavior study of second phase particles in a Zr-Sn-Nb-Fe-Cr-Cu alloy*, J. Nucl. Mater., 423, pp. 127–131.
19. Aldeen, A.W., Chen, Z.W., Disher, I.A., Zhu, Y., Yan, K., 2022, *Growth Kinetics of Second Phase Particles in N36 Zirconium Alloy: Zr-Sn-Nb-Fe*, J. Mater. Res. Technol., 17, pp. 2038-2046.
20. Chai, L.J., Luan, B.F., Gao, S.S., Chen, J.W., Liu, Q., 2012, *Study of precipitate evolution and recrystallization of β-quenched Zr-Sn-Nb-Fe-Cr-Cu alloy during aging*, J. Nucl. Mater., 427, pp. 274-281.
21. Gopalan, P., Rajaraman, R., Amarendra, G., Sundar, C.S., Viswanathan, B., Jayakumar, T., Palanichamy, P., Raj, B., 2005, *Characterisation of β-quenched and thermally aged Zircaloy-2 by positron annihilation, hardness and ultrasonic velocity measurements*, J. Nucl. Mater., 345, pp. 162-166.
22. Jayakumar, S., Ananthapadmanabhan, P.V., Perumal, K., Thiyagarajan, T.K., Mishra, S.C., Su, L.T., Tok, A.I.Y., Guo, J., 2011, *Characterization of nano-crystalline ZrO2 synthesized via reactive plasma processing*, Mater. Sci. Eng. B Solid-State Mater. Adv. Technol., 176, 2011, pp. 894-899.
23. Chai, L., Luan, B., Zhang, M., Murty, K.L., Liu, Q., 2013, *Experimental observation of 12 α variants inherited from one β grain in a Zr alloy*, J. Nucl. Mater., 440, pp. 377-381.
24. Dorić, H., Bolf, N., Šahnić, D., *Development of Crystallization Calibration Model for Real-Time Monitoring of Fosamprenavir Calcium Particle Size Distribution*, Tehnicki Vjesnik, 29, pp. 790-796.
25. Couet, A., Motta, A.T., Ambard, A., Comstock, R.J., 2018, *Hydrogen pickup mechanism in zirconium alloys*, In Comstock, R.J., Motta A.T. (Eds.), *Zirconium in the Nuclear Industry: 18th International Symposium* (pp. 312-349), ASTM Special Technical Publication; Vol. STP 1597, ASTM International. https://doi.org/10.1520/STP159720160055.
26. Garner, A., Gholinia, A., Frankel, P., Gass, M., Maclaren, I., Preuss, M., 2014, *The microstructure and microtexture of zirconium oxide films studied by transmission electron backscatter diffraction and automated crystal orientation mapping with transmission electron microscopy*, Acta Mater., 80, pp. 159-171.
27. Zhang, Q., Huo, X., Li, L., Chen, S., Lu, C., 2022, *Correlation between Precipitation and Recrystallisation during Stress Relaxation in Titanium Microalloyed Steel*, Metals, 12, 1920.
28. Bate, P., 2011, *The effect of deformation on grain growth in Zener pinned systems*, Acta Mater. 49, pp. 1453-1461.
29. Humphreys, F.J., Hatherly, M., 2012, *Recrystallization and related annealing phenomena*, Elsevier, Amsterdam, The Netherlands; Boston, MA, USA.
30. Korznikova, G., Korneva, A., Korznikova, E, 2020, *Application of combined load for obtaining ultra-fine grained structure in magnetic alloys of the Fe-Cr-Co system*, Reports in Mechanical Engineering, 1, pp. 1–9.
31. Yu, J., Yin, Z., Huang, Z., Zhao, S., Huang, H., Yu, K., Zhou, R., Xiao, H., 2022, *Effect of Aging Treatment on Microstructural Evolution and Mechanical Properties of the Electron Beam Cold Hearth Melting Ti-6Al-4V Alloy*, Materials, 15, 7122.
32. Wang, Y., Chai, L., Zhang, F., Chen, K., Guan, H., Luo, J., Li, Y., 2021, *Effects of β-cooling rates on microstructural characteristics and hardness variation of a dual-phase Zr alloy*, Int. J. Refract. Met. Hard Mater. 100, 105619.
33. Prince, M., Vinodh Kumar, A., Mohan Kumar, G., 2022, *Investigation on Mechanical Properties of Aluminum 8011 Metal Matrix Compositewith Titanium Carbide Particulate Reinforcement*, Tehnicki Vjesnik, 29, pp. 2105–2110.
34. Proff, C., Abolhassani, S., Dadras, M.M., Lemaignan, C., 2010, *In situ oxidation of zirconium binary alloys by environmental SEM and analysis by AFM, FIB, and TEM*, J. Nucl. Mater.. 404, pp. 97-108.
35. Abolhassani, S., Dadras, M., Leboeuf, M., Gavillet, D., 2003, *In situ study of the oxidation of Zircaloy-4 by ESEM*, J. Nucl. Mater., 321, pp. 70-77.
36. Park, J.-Y., Choi, B.-K., Yoo, S.J., Jeong, Y.H., *Corrosion behavior and oxide properties of Zr–1.1 wt% Nb–0.05 wt% Cu alloy*, J. Nucl. Mater., 359, pp. 59-68.